

Unsupervised Anomaly Detection of Paranasal Anomalies in the Maxillary Sinus

Debayan Bhattacharya^a, Finn Behrendt^b, Benjamin Tobias Becker^c, Dirk Beyersdorff^d, Elina Petersen^e, Marvin Petersen^f, Bastian Cheng^g, Dennis Eggert^h, Christian Betzⁱ, Anna Sophie Hoffmann^{*j}, and Alexander Schlaefer^{*k}

^{a,b,k}Hamburg University of Technology, Hamburg, Germany
^{a,c,d,e,f,g,h,i,j} Universitätsklinikum Hamburg-Eppendorf, Hamburg, Germany

ABSTRACT

Deep learning (DL) algorithms can be used to automate paranasal anomaly detection from Magnetic Resonance Imaging (MRI). However, previous works relied on supervised learning techniques to distinguish between normal and abnormal samples. This method limits the type of anomalies that can be classified as the anomalies need to be present in the training data. Further, many data points from normal and anomaly class are needed for the model to achieve satisfactory classification performance. However, experienced clinicians can segregate between normal samples (healthy maxillary sinus) and anomalous samples (anomalous maxillary sinus) after looking at a few normal samples. We mimic the clinicians ability by learning the distribution of healthy maxillary sinuses using a 3D convolutional auto-encoder (cAE) and its variant, a 3D variational autoencoder (VAE) architecture and evaluate cAE and VAE for this task. Concretely, we pose the paranasal anomaly detection as an unsupervised anomaly detection problem. Thereby, we are able to reduce the labelling effort of the clinicians as we only use healthy samples during training. Additionally, we can classify any type of anomaly that differs from the training distribution. We train our 3D cAE and VAE to learn a latent representation of healthy maxillary sinus volumes using L1 reconstruction loss. During inference, we use the reconstruction error to classify between normal and anomalous maxillary sinuses. We extract sub-volumes from larger head and neck MRIs and analyse the effect of different fields of view on the detection performance. Finally, we report which anomalies are easiest and hardest to classify using our approach. Our results demonstrate the feasibility of unsupervised detection of paranasal anomalies from MRIs with an AUPRC of 85% and 80% for cAE and VAE, respectively.

Keywords: paranasal anomaly, unsupervised anomaly detection, autoencoder, VAE

1. INTRODUCTION

Anomalies occurring in the paranasal sinuses are commonly reported in patients who undergo neuroradiological assessment of the head using diagnostic imaging.¹ These incidental findings pose clinical challenges² and we have limited knowledge on the importance of these reported findings on the general population. To this end, numerous studies have been done to analyse the significance of these findings.³⁻⁷ Most of these works are population studies involving large sample sizes which are manually annotated by clinicians. In a three year retrospective study, it was observed that malignant tumours and inverted papillomas were classified as nasal polyps with a misdiagnosis rate of 5.63% and 8.45% respectively. Therefore, computer aided diagnosis systems (CADx)⁸⁻¹⁰ have been proposed with the idea of working in conjunction with the clinician to reduce the misdiagnosis rate of paranasal anomalies. However, all these works rely on supervised learning and consider at most one anomaly. Apart from requiring large labelled datasets, supervised learning models also need labelled data that are representative of the classes for accurate prediction.¹¹ Further, the type of anomaly to be classified has to be decided beforehand. In our case, we consider three anomalies, namely: (i) mucosal thickening (ii) polyps (iii) cysts. This is particularly challenging in our case where the considered anomalies are known to have high intra-class morphological variations¹²⁻¹⁴ and have unequal occurrences in our dataset.

Further correspondence, please send an email to: debayan.bhattacharya@tuhh.de

* These authors contributed equally.

In light of the aforementioned points, we are motivated to perform Unsupervised Anomaly Detection (UAD) using autoencoders. Autoencoders are a common choice for data compression and outlier detection.¹⁵ In medical imaging, brain anomaly detection and segmentation¹⁶ has gained popularity over the years. The underlying concept of reconstruction-based UAD is that the autoencoder learns to compress and reconstruct only normal images during training. The assumption is that during testing, reconstruction errors will be low for normal images whereas anomalous images will have a large reconstruction error as the autoencoder will fail to properly reconstruct anomalous regions. In our case, we use cAE and VAE learn to compress and reconstruct healthy maxillary sinus (MS) volumes. Through our approach, we derive multiple benefits, namely: (i) our autoencoder becomes indifferent to the anomaly distribution thereby allowing detection of more than one anomaly, (ii) we reduce the labelling effort of the clinicians as the training dataset does not require anomalous samples, (iii) we are able to generate a heat map based on the reconstruction error between the original volume and the reconstructed volume. The heat maps visualize the region of the potential anomaly and highlight it. This may prove to be beneficial to the clinician when making a diagnosis.

In summary, our contributions are three-fold. First, we pose the paranasal anomaly detection problem as a UAD problem and thereby become indifferent to the anomaly distribution. Second, we systematically evaluate our cAE and VAE approach on MS volumes with different field of view. Third, we report which anomalies are easiest and the hardest to classify using our UAD method.

2. METHODS

2.1 Dataset and Implementation Details

Our labelled dataset consists of head and neck MRIs of 199 patients. Each MRI is a fluid attenuated inversion recovery (FLAIR) MRI. Our labelled dataset is part of the Hamburg City Health Study.¹⁷ Out of the 199 patients, 93 patients exhibit one or multiple anomalies in at least left or right MS. Two Ear, Nose and Throat (ENT) surgeons and one ENT specialised radiologist confirmed the diagnosis of the observed pathology. We group the 3 anomalies into a single class called "anomaly" and the normal MS are categorized into "normal" class. Altogether, we have 269 normal MS volumes and 130 anomalous MS volumes. Each MRI has a resolution of $173 \times 319 \times 319$ voxels along the sagittal, coronal and axial directions respectively with each voxel of size $0.53 \text{ mm} \times 0.75 \text{ mm} \times 0.75 \text{ mm}$.

Preprocessing : We randomly selected a FLAIR MRI as the fixed MRI and performed rigid registration on the remaining MRIs. This was followed by resampling to a dimension of $128 \times 128 \times 128$. We extracted two sub-volumes from the resampled head and neck MRIs, one for each MS. The extracted sub-volumes were of sizes: $33 \times 47 \times 45$ (small), $46 \times 57 \times 55$ (medium) and $53 \times 67 \times 65$ (large). Owing to the symmetry of left and right MS, we horizontally flipped the coronal planes of right MS to give it the appearance of left MS for each patient. Finally, these sub-volumes were reshaped to a standard size of $64 \times 64 \times 64$ voxels for the 3D cAE and VAE. All the MS volumes were normalised to a range of 0 to 1. Our preprocessing pipeline is illustrated in figure 1 (a,b)

Data split: Our training set contains 172 normal MS volumes, validation set contains 43 normal MS volumes and 52 anomalous MS volumes and test set contains 54 normal MS volumes and 78 anomalous MS volumes. We perform a three-fold cross validation split for all our experiments.

Implementation Details: We use PyTorch¹⁸ and PyTorch Lightning¹⁹ for all our experiments. We use batch size $N = 16$ and latent dimension $n_z = 512$ for the cAE. We use a learning rate of $1e^{-4}$ and Adam optimizer²⁰ with default parameters to train our cAE and VAE. We run all our experiments for 100 epochs.

2.2 Deep Learning Methods

Similar to Bengs *et al.*,²¹ we extend our architecture to 3D as it has shown to improve the detection performance in 3D MRI scans. Our cAE and VAE architectures are shown in figure 1 (i). There are two stages to our approach. First, we train our cAE and VAE to learn the distribution of X_h where X_h represents healthy MS volumes. For training our cAE, we use the L1 reconstruction loss as described below:

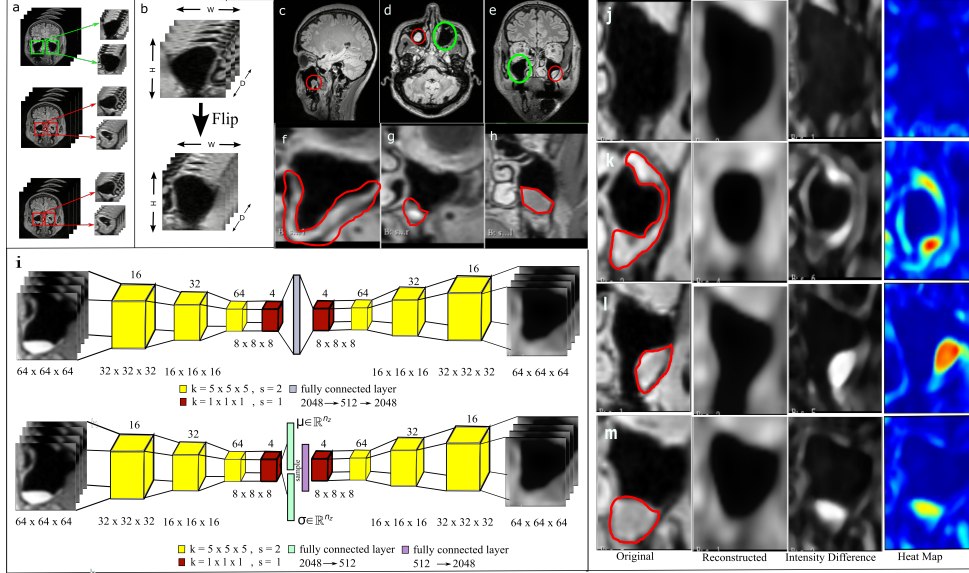


Figure 1. (a) Extraction of left and right MS from head and neck MRI (b) Flipping of the coronal plane of right MS (c) Cyst in the right MS (d) Polyp in the left MS (e) Cyst in the left MS (f) MS (small) showing mucosal thickening (g) MS (medium) showing polyp (h) MS (large) showing cyst (i) TOP: Our cAE architecture with latent vector of size 512 used as bottleneck. BOTTOM: Our VAE architecture. In both the cAE and VAE decoders, we perform 3D convolution followed by trilinear upsampling. ReLU is used as non-linear activation function in both the networks. (j)-(m) Images extracted from original, reconstructed, intensity difference and heat map volumes. (j) is an image extracted from normal MS volume. (k),(l),(m) are mucosal thickening, polyps and cyst anomalies respectively. The red markings denote anomalies and green circles denote normal MS.

$$L_1 = \sum_{k=1}^N |x^k - \hat{x}^k| \quad (1)$$

Here, x^k and \hat{x}^k denote the k -th MS volume and reconstructed MS volume respectively. N denotes the mini-batch size. For training our VAE, we use L1 reconstruction loss and KL Divergence. While training, the VAE learns a mean μ_z and variance σ_z from which a sample is drawn and reconstructed. The loss used to train our VAE is shown below:

$$L_{VAE} = L_1 + \lambda_{KL} D_{KL}(q(z|x)||p(z)) \quad (2)$$

Here, $D_{KL}(\cdot||\cdot)$ represents the Kullback–Leibler divergence between the parameterized latent distribution $q(z|x) \sim N(\mu_z, \sigma_z)$ and the prior $p(z)$ which follows a multivariate normal distribution. $z \in \mathbb{R}^{n_z}$ represents the latent vector. λ_{KL} is a Lagrangian multiplier and we have set it to 1 for our experiments. VAE projects the the input MS volume to $q(z|x)$ and KL-Divergence loss attempts to bring it close to a prior $p(z)$.²²

Second, we use the trained cAE and VAE to reconstruct the MS volumes in the validation set. For each MS volume, we calculate the L1 and L2 reconstruction loss denoted as t_{L1} and t_{L2} respectively. We choose the optimal thresholds by plotting the precision recall curve and select the threshold with the highest F1 score. During inference, \hat{x}^k with $L_1 > t_{L1}$ and $L_2 > t_{L2}$ is classified as anomalous MS volume. Here, L_2 is the L2 reconstruction loss defined as follows:

$$L_2 = \sum_{k=1}^N (x^k - \hat{x}^k)^2 \quad (3)$$

Additionally, for the MS volumes classified as anomalous, a further analysis is done by calculating voxel-wise intensity difference $D_k = |x^k - \hat{x}^k|$ after which a median filter of kernel size 5 is applied on it to remove sporadic

Table 1. Anomaly Detection Performance on two thresholds t_{L1} and t_{L2} where positive labels are assigned to the anomalous class.

Method	MS Size	Precision		Recall		F1		AUPRC	
		t_{L1}	t_{L2}	t_{L1}	t_{L2}	t_{L1}	t_{L2}	t_{L1}	t_{L2}
VAE	small	0.69	0.76	0.63	0.62	0.64	0.68	0.76	0.80
VAE	medium	0.63	0.63	0.84	0.91	0.72	0.75	0.70	0.75
VAE	large	0.61	0.64	0.81	0.86	0.70	0.73	0.65	0.69
cAE	small	0.75	0.81	0.74	0.66	0.74	0.73	0.81	0.83
cAE	medium	0.73	0.77	0.62	0.74	0.67	0.75	0.80	0.85
cAE	large	0.68	0.74	0.82	0.73	0.74	0.73	0.73	0.78

reconstruction errors. Finally, a heat map is rendered for the individual slices along the coronal, axial and sagittal planes as shown in figure 1 (j, k, l, m). The regions in red denote the regions which the cAE failed to reconstruct. Our qualitative results indicate an overlap between the anomalous regions and the poorly reconstructed regions of MS volumes.

3. RESULTS

Table 2. Accuracy per anomaly on the test set reported in percentage (%). Here, # refers to the number of correctly classified samples divided by the total samples from a particular category.

Method	MS Size	Normal (%/#)	Mucosal Thickening (%/#)	Polyps (%/#)	Cysts (%/#)
VAE	small	0.48 (26/54)	0.75 (22/29)	0.82 (28/34)	0.73 (11/15)
cAE	medium	0.61 (33/54)	0.62 (18/29)	0.91 (31/34)	0.8 (12/15)

The anomaly detection performance is shown in table 1. We consider the Area Under Precision Recall Curve (AUPRC) to evaluate our classifiers as we have an unbalanced test set. We rank the classifiers based on AUPRC. We report the mean values of the mentioned metrics. In terms of AUPRC, the VAE that uses small MS volume and cAE that uses medium MS volume are the best performing classifiers.

From table 1, we notice that the all the VAEs have relatively lower AUPRC in comparison to cAEs. Furthermore, our results show that considering L2 loss when computing the anomaly score and using t_{L2} as threshold leads to better performance for all cAEs and VAEs. In table 2, we report the accuracy per anomaly in terms of percentage and number of occurrences for the best performing VAE and cAE from table 1. We observe that polyps are the easiest to classify, followed by cysts. Mucosal thickening anomaly is the hardest to classify for both VAE and cAE.

4. DISCUSSION AND CONCLUSION

From the results in table 1 we observe that using t_{L2} as threshold leads to better performance. This can be attributed to the fact that L2 loss penalizes voxel-wise intensity outliers more heavily than L1 loss. Therefore, even small regions of poor reconstruction in the MS volume can amount to high overall reconstruction error. Additionally, our accuracy percentage per anomaly reported in table 2 shows that mucosal thickening anomalies are the most difficult to classify. We believe this to be the case because unlike polyps and cysts which occur as visible masses in the MRI (See figure 1 (l),(m)), mucosal thickening anomalies have more subtle appearances as these anomalies mostly cause inflammation of the mucosal walls. Therefore, unless the inflammations are too noticeable, they almost have the appearance of a healthy MS. We also observe that classifiers using small and medium MS volumes have the best AUPRCs. This can be attributed to the fact that cropping large volumes lead to inclusion of unnecessary surrounding anatomical structures outside of the MS. These additional anatomical structures effect the reconstruction error and thereby, we end up selecting sub-optimal thresholds. Our work has

some limitations, one being the accuracy of healthy MS volume detection needs to be higher. We think this can be achieved by better localisation and cropping strategies of the MS in the head and neck MRI and by labelling more healthy MS volumes. Second, we have not experimented with autoencoders with skip connections or with more parameters and studied its effect on reconstruction error.

In conclusion, we evaluate UAD for paranasal anomaly detection. Previous methods^{8–10} have used supervised learning methods and as a result are constrained to classify the anomalies that are included in the training distribution. Through our UAD approach, our models learn the healthy MS volume distribution X_h thereby reducing the labelling effort of the clinicians. Also, we are able to detect multiple anomalies. Further, we render heat maps of poor reconstruction. This can provide valuable insights to clinicians while making a diagnosis.

REFERENCES

- [1] Wilson, R., Kuan Kok, H., Fortescue-Webb, D., Doody, O., Buckley, O., and Torreggiani, W. C., “Prevalence and seasonal variation of incidental mri paranasal inflammatory changes in an asymptomatic irish population,” *Irish medical journal* **110**(9), 641 (2017).
- [2] Hansen, A. G., Helvik, A.-S., Nordgård, S., Bugten, V., Stovner, L. J., Håberg, A. K., Gårseth, M., and Eggesbø, H. B., “Incidental findings in mri of the paranasal sinuses in adults: a population-based study (hunt mri),” *BMC ear, nose, and throat disorders* **14**(1), 13 (2014).
- [3] Tarp, B., Fiirgaard, B., Christensen, T., Jensen, J. J., and Black, F. T., “The prevalence and significance of incidental paranasal sinus abnormalities on mri,” *Rhinology* **38**(1), 33–38 (2000).
- [4] Rak, K. M., Newell, J. D., Yakes, W. F., Damiano, M. A., and Luethke, J. M., “Paranasal sinuses on mr images of the brain: significance of mucosal thickening,” *AJR. American journal of roentgenology* **156**(2), 381–384 (1991).
- [5] Stenner, M. and Rudack, C., “Diseases of the nose and paranasal sinuses in child,” *GMS current topics in otorhinolaryngology, head and neck surgery* **13**, Doc10 (2014).
- [6] Rege, I. C. C., Sousa, T. O., Leles, C. R., and Mendonça, E. F., “Occurrence of maxillary sinus abnormalities detected by cone beam ct in asymptomatic patients,” *BMC oral health* **12**, 30 (2012).
- [7] Cooke, L. D. and Hadley, D. M., “Mri of the paranasal sinuses: incidental abnormalities and their relationship to symptoms,” *The Journal of laryngology and otology* **105**(4), 278–281 (1991).
- [8] Kim, Y., Lee, K. J., Sunwoo, L., Choi, D., Nam, C.-M., Cho, J., Kim, J., Bae, Y. J., Yoo, R.-E., Choi, B. S., Jung, C., and Kim, J. H., “Deep learning in diagnosis of maxillary sinusitis using conventional radiography,” *Investigative radiology* **54**(1), 7–15 (2019).
- [9] Jeon, Y., Lee, K., Sunwoo, L., Choi, D., Oh, D. Y., Lee, K. J., Kim, Y., Kim, J.-W., Cho, S. J., Baik, S. H., Yoo, R.-E., Bae, Y. J., Choi, B. S., Jung, C., and Kim, J. H., “Deep learning for diagnosis of paranasal sinusitis using multi-view radiographs,” *Diagnostics (Basel, Switzerland)* **11**(2) (2021).
- [10] Liu, G. S., Yang, A., Kim, D., Hojel, A., Voevodsky, D., Wang, J., Tong, C. C. L., Ungerer, H., Palmer, J. N., Kohanski, M. A., Nayak, J. V., Hwang, P. H., Adappa, N. D., and Patel, Z. M., “Deep learning classification of inverted papilloma malignant transformation using 3d convolutional neural networks and magnetic resonance imaging,” *International forum of allergy & rhinology* (2022).
- [11] Althnian, A., AlSaeed, D., Al-Baity, H., Samha, A., Dris, A. B., Alzakari, N., Abou Elwafa, A., and Kurdi, H., “Impact of dataset size on classification performance: An empirical evaluation in the medical domain,” *Applied Sciences* **11**(2) (2021).
- [12] Tos, M., Larsen, P. L., Larsen, K., and Cayé-Thomasen, P., [*Nasal Polyps*], 103–125, Springer Berlin Heidelberg, Berlin, Heidelberg (2000).
- [13] Janner, S. F. M., Caversaccio, M. D., Dubach, P., Sendi, P., Buser, D., and Bornstein, M. M., “Characteristics and dimensions of the schneiderian membrane: a radiographic analysis using cone beam computed tomography in patients referred for dental implant surgery in the posterior maxilla,” *Clin Oral Implants Res* **22**, 1446–1453 (Mar. 2011).
- [14] Hung, K., Hui, L., Yeung, A. W. K., Wu, Y., Hsung, R. T.-C., and Bornstein, M. M., “Volumetric analysis of mucous retention cysts in the maxillary sinus: A retrospective study using cone-beam computed tomography,” *Imaging Sci Dent* **51**, 117–127 (Jan. 2021).

- [15] Pang, G., Shen, C., Cao, L., and Hengel, A. V. D., “Deep learning for anomaly detection: A review,” *ACM Comput. Surv.* **54** (mar 2021).
- [16] Baur, C., Denner, S., Wiestler, B., Navab, N., and Albarqouni, S., “Autoencoders for unsupervised anomaly segmentation in brain mr images: A comparative study,” *Medical Image Analysis* , 101952 (2021).
- [17] Jagodzinski, A., Johansen, C., Koch-Gromus, U., Aarabi, G., Adam, G., Anders, S., Augustin, M., der Kellen, R. B., Beikler, T., Behrendt, C.-A., Betz, C. S., Bokemeyer, C., Borof, K., Briken, P., Busch, C.-J., Büchel, C., Brassens, S., Debus, E. S., Eggers, L., Fiehler, J., Gallinat, J., Gellißen, S., Gerloff, C., Girdauskas, E., Gosau, M., Graefen, M., Härter, M., Harth, V., Heidemann, C., Heydecke, G., Huber, T. B., Hussein, Y., Kampf, M. O., von dem Knesebeck, O., Konnopka, A., König, H.-H., Kromer, R., Kubisch, C., Kühn, S., Loges, S., Löwe, B., Lund, G., Meyer, C., Nagel, L., Nienhaus, A., Pantel, K., Petersen, E., Püschel, K., Reichenspurner, H., Sauter, G., Scherer, M., Scherschel, K., Schiffner, U., Schnabel, R. B., Schulz, H., Smeets, R., Sokalskis, V., Spitzer, M. S., Terschüren, C., Thederan, I., Thoma, T., Thomalla, G., Waschki, B., Wegscheider, K., Wenzel, J.-P., Wiese, S., Zyriax, B.-C., Zeller, T., and Blankenberg, S., “Rationale and design of the hamburg city health study,” *European Journal of Epidemiology* **35**, 169–181 (Feb 2020).
- [18] Paszke, A., Gross, S., Massa, F., Lerer, A., Bradbury, J., Chanan, G., Killeen, T., Lin, Z., Gimelshein, N., Antiga, L., Desmaison, A., Köpf, A., Yang, E., DeVito, Z., Raison, M., Tejani, A., Chilamkurthy, S., Steiner, B., Fang, L., Bai, J., and Chintala, S., “Pytorch: An imperative style, high-performance deep learning library.”
- [19] Falcon et al., W., “Pytorch lightning,” *GitHub*. Note: <https://github.com/PyTorchLightning/pytorch-lightning> **3** (2019).
- [20] Kingma, D. P. and Ba, J., “Adam: A method for stochastic optimization,” (2014).
- [21] Bengs, M., Behrendt, F., Krüger, J., Opfer, R., and Schlaefer, A., “Three-dimensional deep learning with spatial erasing for unsupervised anomaly segmentation in brain mri,” *CARS* , 1–11 (2021).
- [22] Kingma, D. P. and Welling, M., “Auto-encoding variational bayes,” (2013).